JGR Oceans

RESEARCH ARTICLE
10.1029/2025JC022880

Impact of Topography on Submesoscale Ageostrophic Kinetic Energy in the Kuroshio South of Japan

Zheyue Shen[1,2], **Yang Yang**[3], **Jianyu Hu**[3], **and Shuwen Zhang**[1,2]

[1]Institute of Marine Science, Shantou University, Shantou, China, [2]Guangdong Provincial Key Laboratory of Marine Disaster Prediction and Protection, Shantou University, Shantou, China, [3]State Key Laboratory of Marine Environmental Science, Center for Marine Meteorology and Climate Change, College of Ocean and Earth Sciences, Xiamen University, Xiamen, China

Key Points:

- Submesoscale ageostrophic kinetic energy (KE) is pronounced around the Izu-Ogasawara Islands in the Kuroshio south of Japan
- Ageostrophic motion and its interaction with geostrophic flow dominate background KE transfers to the submesoscales around the islands
- Away from the islands, a weak inverse KE cascade occurs, with submesoscale KE sourced from the conversion of available potential energy

Correspondence to:
S. Zhang,
zhangsw@stu.edu.cn

Citation:
Shen, Z., Yang, Y., Hu, J., & Zhang, S. (2025). Impact of topography on submesoscale ageostrophic kinetic energy in the Kuroshio south of Japan. *Journal of Geophysical Research: Oceans*, *130*, e2025JC022880. https://doi.org/10.1029/2025JC022880

Received 14 MAY 2025
Accepted 28 SEP 2025

Author Contributions:
Formal analysis: Yang Yang
Investigation: Jianyu Hu
Writing – original draft: Zheyue Shen
Writing – review & editing: Shuwen Zhang

Abstract The submesoscale energetics over the topography in the Kuroshio south of Japan are analyzed using the 1/48° resolution MITgcm LLC-4320 simulation. We use the multiscale window transform (MWT) and canonical transfer theory based on MWT to investigate the cross-scale kinetic energy (KE) transfers between the background flow and submesoscale currents, and the conversion of submesoscale available potential energy (SAPE) to KE. Results show that ageostrophic KE predominates on the submesoscale window near the Izu-Ogasawara Islands, peaking in August while reaching a minimum in March. In August, the Kuroshio follows a nearshore path with high background KE, generating ageostrophic centrifugal instability as it crosses the islands. This instability is accompanied by significant ageostrophic motions and interactions between geostrophic and ageostrophic flows. As a result, two types of KE transfers from the background flow to submesoscale windows are generated: the ageostrophic KE cascade and the transfer associated with geostrophic-ageostrophic current interactions. In contrast, in March, the Kuroshio follows an offshore path with weaker KE background, leading to a reduction in KE transfer. The conversion from SAPE to KE remains negligible during these 2 months. However, in the region farther from the islands where a weak inverse KE transfer predominates, the submesoscale ageostrophic KE is relatively small; and SAPE is the main source of submesoscale KE in March, but not in August. Our results highlight the role of ageostrophic motions and their interactions with geostrophic flows in cross-scale KE cascades, contributing to a quantitative understanding of complex submesoscale dynamics in island areas.

Plain Language Summary The Izu-Ogasawara Islands lie south of Japan, where the Kuroshio passes through. As an oceanic background circulation, the Kuroshio satisfies geostrophic balance, and most of the kinetic energy (KE) is stored in the geostrophic KE. Due to Kuroshio-topography interactions and the loss of geostrophic balance, the island region is characterized by pronounced submesoscale processes and high submesoscale ageostrophic KE. Ageostrophic motions, along with their interactions with geostrophic motions, extract KE from the background flow and transfer it to submesoscale ageostrophic KE. The contribution of the Kuroshio background flow and its path across the islands varies seasonally, leading to changes in the submesoscale ageostrophic KE in the region around the islands. Our analysis of cross-scale KE transfers in the island region reveals that ageostrophic motions and their interactions with geostrophic flows significantly contribute to submesoscale ageostrophic KE. In addition, submesoscale processes play a crucial role in the forward KE transfer from the geostrophic scale toward dissipation.

1. Introduction

The submesoscale processes, with a horizontal scale of $O(0.1–10)$ km and a timescale ranging from a few hours to several weeks, are ubiquitous in the ocean. These processes are intermediate between mesoscale and small-scale processes, possessing unique dynamic characteristics. Submesoscale processes are commonly found in western boundary current regions, with both geostrophic and ageostrophic components coexisting (D'Asaro et al., 2011; Qiu et al., 2017; Zhang & Qiu, 2018).

Mesoscale processes, governed by quasi-geostrophic dynamics, tend to transfer energy inversely to larger scales while the ageostrophic nature of submesoscale motions drives a forward cascade toward dissipation (Arbic et al., 2012; Ferrari & Wunsch, 2009; Jing et al., 2021; McWilliams, 2016; Qiu et al., 2022). This ageostrophic nature also exhibits several significant characteristics, including intense upwelling/downwelling and rapid restratification (McWilliams, 2017; Thomas, 2008; Thomas et al., 2008; Yang et al., 2021; Zhang et al., 2019).

Flow-topography interaction is one of the important generation mechanisms of submesoscale processes (Gula et al., 2015; Srinivasan et al., 2019; Zhang, 2024; Zhang et al., 2022). Submesoscale currents, which carry marked KE, are often found near steep topographies, such as continental slopes, seamounts, and ridges (Chen et al., 2024; Molemaker et al., 2015; Ruan et al., 2017). A series of high-resolution numerical model simulations have emphasized that submesoscale currents are generated through the interactions between geostrophic flows and steep topographic slopes (Napolitano et al., 2020; Naveira Garabato et al., 2019; Perfect et al., 2018; Srinivasan et al., 2017).

The dynamic transition from large-scale and mesoscale to submesoscale motions is typically accompanied by a disruption of geostrophic balance and the generation of ageostrophic motions (Dong et al., 2007; Grooms, 2015; Mahadevan & Tandon, 2006).

On sloping seafloors, topographic drag can induce vertical and horizontal shears in background ocean currents, which may cause the shear currents to separate from the turbulent bottom boundary layers (Srinivasan et al., 2019). These shear currents, which break the constraints of the bottom boundary layers, may undergo a series of ageostrophic instabilities, including baroclinic instability, centrifugal instability, or horizontal shear instability. Ageostrophic instabilities could serve as a mechanism directly linking balanced mesoscale dynamics with unbalanced submesoscale motions (Dewar et al., 2015; Gula et al., 2016; McWilliams, 2016).

As a strong western boundary current in the North Pacific, the Kuroshio regulates material transport and heat exchange, also playing a key role in the distribution of momentum in the North Pacific Ocean (Soeyanto et al., 2014; Wang et al., 2016). The Izu-Ogasawara Ridge is located to the south of Japan, connecting the Izu Islands and the Ogasawara Islands. It extends from Japan's Izu Peninsula to a region near the Mariana Trench. After crossing the Izu-Ogasawara Ridge region, the Kuroshio tends to experience mixing and instability (Hasegawa et al., 2004; Nagai et al., 2017; Tsutsumi et al., 2017). The interaction between the Kuroshio and the Izu-Ogasawara Ridge generates submesoscale KE primarily through barotropic instability while baroclinic instability is suppressed (Masunaga et al., 2022). Simultaneously, the topography around the Izu-Ogasawara Ridge is closely related to changes in the Kuroshio's path and exerts a notable controlling effect on the structure of the Kuroshio (Sekine, 1990; Sekine & Toba, 1981).

When the Kuroshio follows different paths across the island region over the Izu-Ogasawara Ridge, its geostrophic balance is disrupted by the unique topography. As a background flow, how does the Kuroshio interact with submesoscale processes, leading to the generation of ageostrophic KE at the submesoscale? The exploration of this interaction will facilitate a quantitative discussion of the complex submesoscale dynamics.

The remainder of this paper is organized as follows. Section 2 provides a brief introduction to the data and methods used in this study. Section 3 presents the KE, geostrophic KE, and ageostrophic KE at multiple scales in the Kuroshio south of Japan. Section 4 focuses on the analysis of the processes involved in submesoscale KE transfers within the selected area. Section 5 analyzes the mechanism of ageostrophic instability in the study area. Finally, Section 6 contains the discussion, and the main findings of this study are summarized in Section 7.

2. Data and Methods

2.1. Topographic Data and MIT LLC-4320 Simulation

The Earth TOPOgraphy 2022 (ETOPO 2022) is a global data set that includes bathymetric, topographic, and coastline data, made available by the National Oceanic and Atmospheric Administration (NOAA, 2022, https://www.ncei.noaa.gov/products/etopo-global-relief-model). The data set is composed of 288 individual 15° × 15° grid sections (longitude/latitude), each with a geographic resolution of 15 arc-seconds, providing a high-resolution comprehensive representation of the Earth's physical characteristics.

The global high-resolution LLC-4320 (Latitude-Longitude-polar Cap 4320) model data set, developed by the General Circulation team at the Massachusetts Institute of Technology (MITgcm), is accessible through the National Aeronautics and Space Administration (NASA) research center (https://data.nas.nasa.gov/ecco). The model data set features a horizontal resolution of up to 1/48° and includes 90 vertical levels. The vertical resolution varies from 1 m at the sea surface to 480 m at the seafloor. The model is forced by the European Centre for Medium-Range Weather Forecasts (ECMWF) Atmospheric Reanalysis Data, with a resolution of 0.14° and updated every 6 hr. The atmospheric forcing field reanalysis data encompass variables such as 10-m wind speed,

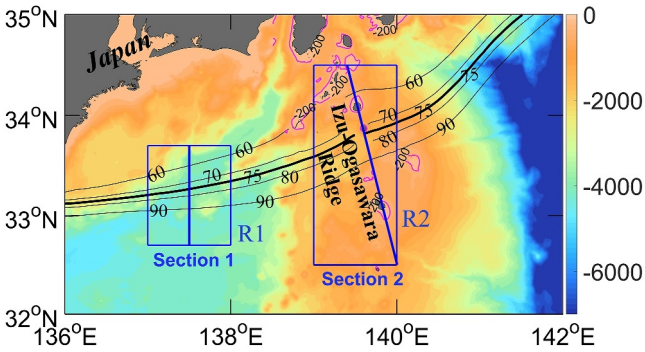

Figure 1. Bathymetry (color shading, units: m) overlaid with mean sea surface height (SSH) for November 2011–October 2012, represented by thin black contours at 10 cm intervals, ranging from 60 to 90 cm. The thick black line indicates the main axis of the Kuroshio (defined by the 75-cm SSH contour). Blue boxes represent: region R1 (32.7°–33.7°N, 137°–138°E) and region R2 (32.5°–34.5°N, 139°–140°E), respectively. Section 1 (solid blue line) in region R1 is located at longitude 137.5°E, spanning from 32.7°N to 33.7°N. Section 2 (solid blue line) in region R2 is defined by the two endpoints: (140.0°E, 32.5°N) and (139.4°E, 34.5°N). Pink lines indicate the 200-m isobaths.

2-m temperature and humidity, longwave and shortwave radiations, atmospheric pressure, and others. The model is simulated from September 2011 to November 2012. The data utilized in this study cover the period from November 2011 to October 2012, with an hourly temporal resolution. The physical variables include sea surface height (SSH; η), potential temperature (T), salinity (S), zonal velocity (u_T), meridional velocity (v_T), and vertical velocity (w_T). To remove most of the unbalanced internal gravity waves unassociated with submesoscale processes (e.g., Su et al., 2018), we apply a 24-hr low-pass filter to all aforementioned variables before conducting the analyses.

The Kuroshio is a well-known western boundary current in the North Pacific Ocean.

As shown in Figure 1, the Kuroshio flows northeastward to the south of Japan, crossing the island region over the Izu-Ogasawara Ridge.

2.2. Methods

2.2.1. Geostrophic and Ageostrophic Currents

The sea surface layer geostrophic currents are calculated from the SSH (η):

$$u_0 = -\frac{g}{f}\frac{\partial \eta}{\partial y} \tag{1}$$

$$v_0 = \frac{g}{f}\frac{\partial \eta}{\partial x} \tag{2}$$

here, u_0 and v_0 represent the zonal and meridional components of the sea surface geostrophic currents, respectively; g is the gravitational acceleration; and f represents the Coriolis parameter. Based on the sea surface geostrophic currents, we further calculate the geostrophic currents at the depth z_i:

$$u_G(z_i) = u_0 - \frac{g}{\rho_0 f}\int_{z=z_i}^{z=0}\frac{\partial}{\partial y}\rho(z)\,dz \tag{3}$$

$$v_G(z_i) = v_0 + \frac{g}{\rho_0 f}\int_{z=z_i}^{z=0}\frac{\partial}{\partial x}\rho(z)\,dz \tag{4}$$

$u_G(z_i)$ and $v_G(z_i)$ represent the zonal and meridional components of the geostrophic currents at the depth z_i, respectively (Mulet et al., 2012). ρ_0 and $\rho(z)$ denote the reference seawater density of 1,024 kg/m^3 and the seawater density at the depth $z = z_i$, respectively. The ageostrophic currents, $u_A(z_i)$ and $v_A(z_i)$, are obtained by subtracting the geostrophic currents, $u_G(z_i)$ and $v_G(z_i)$, from the total velocities, $u_T(z_i)$ and $v_T(z_i)$.

2.2.2. Geostrophic Richardson Number and Ertel Potential Vorticity

The geostrophic Richardson number R_{ig} is an important parameter for analyzing fluid instability (Stone, 1966, 1970). When the logarithm of the R_{ig} is large, fluid instability is less prone to occur, whereas a small logarithm of the R_{ig} increases the likelihood of fluid instability (Abarbanel et al., 1984; Galperin et al., 2007; Thomas et al., 2013). The geostrophic Richardson number is expressed as follows:

$$R_{ig} = \frac{f^2 N^2}{|\nabla_h b|^2} \tag{5}$$

where $\nabla_h b$ represents the horizontal buoyancy gradient, with $b = -g\frac{\rho}{\rho_0}$, and N^2 is the square of the buoyancy frequency.

Table 1
The Mathematical Expressions and Physical Interpretations of the Energy Terms, Refer to Liang (2016) for Further Details

Terms	Mathematical expression	Meaning
$\nabla\cdot\mathbf{Q}_K^{\varpi}$	$\nabla\cdot\left[\frac{1}{2}\widehat{(\mathbf{v}\mathbf{v}_h)}^{\sim\varpi}\cdot\hat{\mathbf{v}}_h{}^{\sim\varpi}\right]$	The advection of KE on window ϖ
Γ^{ϖ}	$\frac{1}{2}\left[\widehat{(\mathbf{v}\mathbf{v}_h)}^{\sim\varpi}:\nabla\hat{\mathbf{v}}_h{}^{\sim\varpi}-\nabla\cdot\widehat{(\mathbf{v}\mathbf{v}_h)}^{\sim\varpi}\cdot\hat{\mathbf{v}}_h{}^{\sim\varpi}\right]$	Canonical KE transfer on window ϖ
$\nabla\cdot\mathbf{Q}_P^{\varpi}$	$\nabla\cdot\left(\frac{1}{\rho_0}\hat{\mathbf{v}}^{\sim\varpi}\hat{P}^{\sim\varpi}\right)$	Pressure forces work on window ϖ
b^{ϖ}	$\frac{g}{\rho_0}\hat{\rho}^{\sim\varpi}\hat{w}^{\sim\varpi}$	Buoyancy conversion on window ϖ; negative b^{ϖ} means a conversion of available potential energy to KE on window ϖ
F_K^{ϖ}	Implicitly accounted for and considered as a residual term in the KE budget equation	Change rate of KE caused by wind stress and internal dissipation on window ϖ

As a fundamental diagnostic for dynamic instability, Ertel potential vorticity (PV) is intrinsically linked to submesoscale processes (Thomas et al., 2013). A necessary condition for the development of fluid dynamical instability is the reversal of the sign between the Ertel PV and the Coriolis parameter (Hoskins, 1974). Ertel PV is defined as follows:

$$q=\boldsymbol{\omega}_a\cdot\nabla b \tag{6}$$

The expression $\boldsymbol{\omega}_a=f\mathbf{z}+\nabla\times\mathbf{u}$ defines the absolute vorticity, where $\mathbf{z}$ is the local vertical unit vector and $\mathbf{u}$ is the velocity vector.

2.2.3. Multiscale Window Transform and Canonical Transfer

In this study, we use a temporal decomposition technique, namely, the multiscale window transform (MWT), to decompose the original field to a background field and a submesoscale field. The MWT is developed by Liang and Anderson (2007) for the purpose of obtaining physically consistent multiscale energies. Although filters can be used to fulfill scale separation, defining the energy of the filtered field is by no means trivial. Liang and Anderson (2007) proved that for a class of specially designed orthogonal filters with a wavelet basis, there exists a localized transform coefficient $\hat{u}_n^{\sim\varpi}$ (n denotes the discrete temporal localization) for each filtered field $u^{\sim\varpi}(t)$. The operator $\widehat{(\cdot)}_n^{\sim\varpi}$ is the very MWT. They also proved that the energy on window ϖ is proportional to $\left(\hat{u}_n^{\sim\varpi}\right)^2$.

Using MWT, the KE on scale window ϖ can be derived as $K^{\varpi}=\frac{1}{2}\hat{\mathbf{v}}_h{}^{\sim\varpi}\cdot\hat{\mathbf{v}}_h{}^{\sim\varpi}$, with the governing equation for KE given by:

$$\frac{\partial K^{\varpi}}{\partial t}=\underbrace{-\nabla\cdot\left[\frac{1}{2}\widehat{(\mathbf{v}\mathbf{v}_h)}^{\sim\varpi}\cdot\hat{\mathbf{v}}_h{}^{\sim\varpi}\right]}_{-\nabla\cdot\mathbf{Q}_K^{\varpi}}+\underbrace{\frac{1}{2}\left[\widehat{(\mathbf{v}\mathbf{v}_h)}^{\sim\varpi}:\nabla\hat{\mathbf{v}}_h{}^{\sim\varpi}-\nabla\cdot\widehat{(\mathbf{v}\mathbf{v}_h)}^{\sim\varpi}\cdot\hat{\mathbf{v}}_h{}^{\sim\varpi}\right]}_{\Gamma^{\varpi}}\underbrace{-\nabla\cdot\left(\frac{1}{\rho_0}\hat{\mathbf{v}}^{\sim\varpi}\hat{P}^{\sim\varpi}\right)}_{-\nabla\cdot\mathbf{Q}_P^{\varpi}}$$
$$\underbrace{-\left(\frac{g}{\rho_0}\hat{\rho}^{\sim\varpi}\hat{w}^{\sim\varpi}\right)}_{b^{\varpi}}+F_K^{\varpi} \tag{7}$$

The colon operator is defined as follows: for two dyadic products AB and CD, (AB):(CD) = (A · C) (B · D). The expressions and meanings for each term on the right-hand side of Equation 7 are listed in Table 1.

Among the multiple terms on the right-hand side of Equation 7, Γ^{ϖ} holds particular significance, as it characterizes the cross-scale KE transfer between the background flow and the submesoscale windows. It satisfies an important conservation property, described as follows:

$$\sum_n \sum_{\varpi} \Gamma_n^{\varpi} = 0 \tag{8}$$

Here, $\sum_n$ and $\sum_{\varpi}$ denote summations over all the sampling time steps n and scale windows ϖ, respectively. Note that the subscript n, denoting the discrete time step, is omitted in Equation 7 for brevity. This means that Γ^{ϖ} serves solely to redistribute energy among scales, without creating or destroying energy as a whole. This property is absent in conventional energetics formulations. Interested readers are referred to Yang et al. (2024) for a detailed comparison. To distinguish, Γ^{ϖ} is formally designated as canonical transfer (Liang, 2016). Γ^{ϖ} can be expanded as follows:

$$\Gamma^{\varpi} = \frac{1}{2}\left\{\widehat{(\mathbf{v}u)}^{\sim\varpi}\nabla\hat{u}^{\sim\varpi} - \left[\nabla\cdot\widehat{(\mathbf{v}u)}^{\sim\varpi}\right]\hat{u}^{\sim\varpi}\right\} + \frac{1}{2}\left\{\widehat{(\mathbf{v}v)}^{\sim\varpi}\nabla\hat{v}^{\sim\varpi} - \left[\nabla\cdot\widehat{(\mathbf{v}v)}^{\sim\varpi}\right]\hat{v}^{\sim\varpi}\right\} \tag{9}$$

Note that Γ^{ϖ} not only includes cross-scale transfers between different scale windows but also transfers within the window itself (as each scale window consists of a range of scales). Therefore, Γ^{ϖ} requires further decomposition, which is achieved through the "interaction analysis" procedure detailed by Liang and Robinson (2007). We provide a concise description of this procedure below. Crucially, all terms in Equation 9 exhibit a form of triple product, $\Gamma^{\varpi} = \hat{\xi}^{\sim\varpi}\widehat{(\varphi\psi)}^{\sim\varpi}$. Considering window $\varpi = 1$ (the primary focus of this investigation) as an exemplar, the decomposition proceeds as

$$\Gamma^1 = \hat{\xi}^{\sim 1}\widehat{(\varphi\psi)}^{\sim 1} \tag{10}$$

$$= \underbrace{\hat{\xi}^{\sim 1}\left[\left(\varphi^{\sim 0}\widehat{\psi^{\sim 0}}\right)^{\sim 1} + \left(\varphi^{\sim 0}\widehat{\psi^{\sim 1}}\right)^{\sim 1} + \left(\varphi^{\sim 1}\widehat{\psi^{\sim 0}}\right)^{\sim 1}\right]}_{\Gamma^{0\to 1}} + \underbrace{\hat{\xi}^{\sim 1}\left(\varphi^{\sim 1}\widehat{\psi^{\sim 1}}\right)^{\sim 1}}_{\Gamma^{1\to 1}} \tag{11}$$

The two terms $\Gamma^{0\to 1}$ and $\Gamma^{1\to 1}$ indicate that the KE transfers to scale window 1 from window 0 and within itself, respectively. We will focus on $\Gamma^{0\to 1}$ because it represents the interaction between the background flow and the submesoscale processes.

Following previous studies (e.g., Yang et al., 2021; Zhang et al., 2020), we define the submesoscale as processes with periods shorter than 8 days and longer than 1 day. Processes with a period longer than 8 days are defined as the background flow. At the same time, the MWT is applied to three velocity components: (a) the total velocity (u_T, v_T, w_T), (b) the geostrophic velocity (u_G, v_G), and (c) the ageostrophic velocity (u_A, v_A), in order to obtain the corresponding components of each velocity for the background flow and submesoscale windows. Accordingly, the background and submesoscale KE are derived from the respective components of the total velocity field, following the formalism of Liang (2016). Similarly, the geostrophic and ageostrophic KE are computed within each window from their associated velocity fields.

To validate our decomposition results, we calculate the area-mean submesoscale ageostrophic KE over the study domain (32°–35°N, 136°–142°E) using the MWT method and a spatial high-pass filter with a 50 km cutoff scale (Figure 2). The latter is commonly used to separate submesoscale motions from mesoscale and large-scale processes (Su et al., 2018). The correlation between the two time series is 0.98, which demonstrates that our temporal approach is indeed able to select out the submesoscale motions, consistent with previous studies (e.g., Yang et al., 2021; Zhang et al., 2020). However, we caution that the so-defined "submesoscale" window in this study could also incorporate other high-frequency motions such as moderate-size mesoscale signals.

Additionally, based on Equations 9–11, the canonical transfer corresponding to different velocity components within each window is also calculated. By applying the two-scale window decomposition mentioned above, we are able to diagnose the cross-scale interactions between the background flow and submesoscale motions. Γ^1 includes KE transfer from the background flow window, as well as the transfer information within its own scale window, as shown below:

$$\Gamma^1 = \Gamma^{0\to 1} + \Gamma^{1\to 1} \tag{12}$$

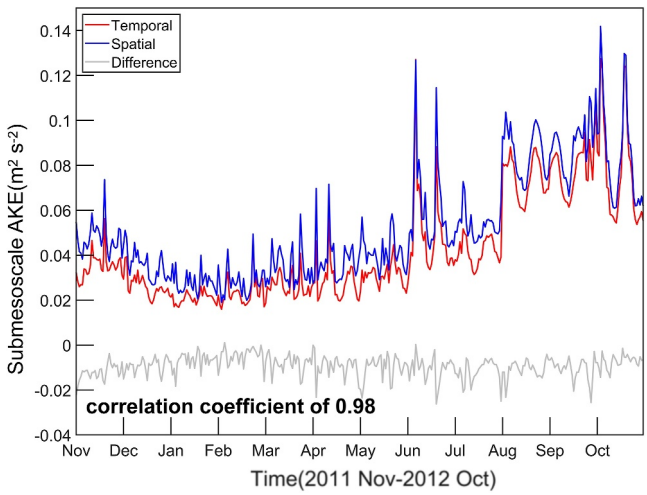

Figure 2. Time series of sea surface ageostrophic KE (AKE, units: $m^2\ s^{-2}$) on the submesoscale window, averaged over the study domain (32°–35°N, 136°–142°E) based on multiscale window transform with cutoff periods between 1 and 8 days (red line) and spatial filtering with a cutoff scale of 50 km (blue line). The gray line represents the difference between the two methods.

For convenience, we use the $\Gamma^{0\to1}$ to denote the canonical transfer of KE from the background flow window ($\varpi = 0$) to the submesoscale window ($\varpi = 1$). A positive $\Gamma^{0\to1}$ means a forward KE transfer from the background flow to the submesoscales, and vice versa. $\Gamma^{1\to1}$ represents KE transfer within the submesoscale window. Since the magnitude of $\Gamma^{1\to1}$ is relatively small, it is not considered in this study. To reveal the relative contributions of geostrophic and ageostrophic motions to the cross-scale KE transfer, we further decompose $\Gamma^{0\to1}$ as

$$\Gamma^{0\to1} = \Gamma_G^{0\to1} + \Gamma_A^{0\to1} + \Gamma_{GA}^{0\to1} \tag{13}$$

Where $\Gamma_G^{0\to1}$ ($\Gamma_A^{0\to1}$) is calculated using only the geostrophic (ageostrophic) velocity, and the cross-term $\Gamma_{GA}^{0\to1}$ is obtained through $\Gamma^{0\to1} - \Gamma_G^{0\to1} - \Gamma_A^{0\to1}$. The three decomposed terms can be interpreted as follows. $\Gamma_G^{0\to1}$ ($\Gamma_A^{0\to1}$) denotes the cross-scale KE transfer from background geostrophic (ageostrophic) flow to submesoscale geostrophic (ageostrophic) current. $\Gamma_{GA}^{0\to1}$ denotes the cross-scale KE transfer due to interactions between geostrophic and ageostrophic flows.

3. Spatiotemporal Characteristics

3.1. Spatial Distributions of Multiscale Geostrophic and Ageostrophic Kinetic Energy

Figure 3 shows the time-averaged distributions of KE, geostrophic KE, and ageostrophic KE for both the background flow and submesoscale windows, averaged over the upper 200 m in the study domain. Overall, the magnitude and distribution patterns of background geostrophic KE are generally consistent with those of background KE (Figures 3a and 3c). This indicates that the Kuroshio on the background flow window largely adheres to geostrophic balance, with most of its KE concentrated in the background geostrophic flow. Background geostrophic KE is the predominant contributor to background KE. High values of ageostrophic KE on the background flow window are observed only around the islands over the Izu-Ogasawara Ridge (Figure 3e). On the submesoscale window, ageostrophic KE is most prominent (Figure 3f). Only small fractions of submesoscale KE and geostrophic KE are concentrated around the Izu-Ogasawara Islands (Figures 3b and 3d).

3.2. Seasonal Features of Submesoscale Ageostrophic Kinetic Energy

The submesoscale ageostrophic motions in the study domain are mainly active near the Izu-Ogasawara Islands. Snapshots of the Rossby number ($R_O = \zeta/f$; $\zeta = \partial v/\partial x - \partial u/\partial y$ is the relative vorticity) at the sea surface on 15 March (a typical winter day) and 15 August (a typical summer day) are shown in Figures 4a and 4b. Large R_O values are concentrated near the Izu-Ogasawara Islands, consistent with the elevated submesoscale ageostrophic KE in this region.

To further investigate the regional signatures of submesoscale ageostrophic KE in the study domain, we select two study areas: one farther from the Izu-Ogasawara Islands and the other closer to it. The selected areas are: region R1 (32.7°–33.7°N, 137°–138°E) and region R2 (32.5°–34.5°N, 139°–140°E) (Figures 1 and 4).

The submesoscale ageostrophic KE in region R2 is notably higher than that in region R1 (Figure 4c). The submesoscale ageostrophic KE in region R2 exhibits a relatively strong seasonal cycle, weakening significantly from winter to spring and reaches its minimum value of approximately 0.07 $m^2\ s^{-2}$ in early spring, around March. The submesoscale ageostrophic KE in this region increases markedly and peaks at approximately 0.21 $m^2\ s^{-2}$ in August. The seasonal variation of submesoscale ageostrophic KE in region R1 is less pronounced than in region R2, but it still shows a slight weakening during the winter and a slight increase during the summer. In March, as the main axis of the Kuroshio follows an offshore, meandering path across the Izu-Ogasawara Ridge, high values of submesoscale ageostrophic KE are sparsely distributed around the islands along the ridge (Figure 4d). In

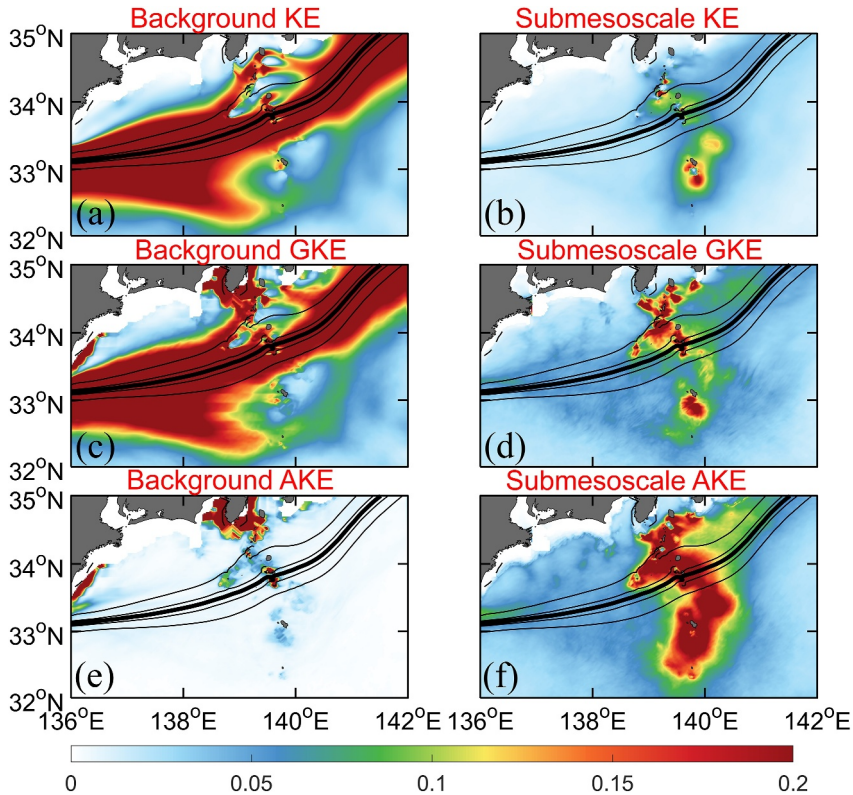

Figure 3. Kinetic energy (KE) (color shading, units: $m^2\ s^{-2}$) for background flow and submesoscale windows in the study domain (32°–35°N, 136°–142°E), averaged over the upper 200 m from November 2011 to October 2012. Panels (a, c, and e) show the background KE, geostrophic KE (GKE), and ageostrophic KE (AKE), respectively, while Panels (b, d, and f) present their submesoscale counterparts. The mean sea surface height (SSH) (averaged from November 2011 to October 2012, units: cm) is overlaid as contours, with thin black lines indicating 60–90 cm in 10 cm intervals, and the thick black contour indicates the main axis of the Kuroshio (defined by the 75-cm SSH contour).

August, as the main axis of the Kuroshio follows a nearshore and relatively straight path over the Izu-Ogasawara Ridge, pronounced submesoscale ageostrophic KE is widely distributed, nearly covering the entire island region (Figure 4e).

This study will focus on analyzing how the Izu-Ogasawara Islands influence submesoscale ageostrophic KE in the study domain during March and August.

4. Submesoscale Energetics Analysis

4.1. Buoyancy Conversion

It is worth noting that b^1 is related to the conversion from SAPE to submesoscale KE driven by baroclinic instability. And it is also closely associated with ageostrophic perturbations (Capet et al., 2008; McWilliams, 2016, 2019). In this study, a negative b^1 indicates a transfer of SAPE to submesoscale KE while a positive b^1 signifies a transfer of submesoscale KE back to SAPE. In region R1, located away from the Izu-Ogasawara Islands, b^1 is predominantly negative and distributed along the main axis of the Kuroshio in March. In region R2, notable b^1 is primarily located on the northern side of the Izu-Ogasawara Islands, exhibiting a spatial pattern of alternating positive and negative values (Figure 5a). In August, substantial b^1 values in region R2 extend over much of the island region along the Izu-Ogasawara Ridge, with predominantly positive values reaching up to $1.0 \times 10^{-4}\ m^3\ s^{-3}$. In contrast, b^1 in region R1 is relatively weaker, exhibiting a pattern of alternating positive and negative values, with magnitudes reaching only $\pm 0.2 \times 10^{-4}\ m^3\ s^{-3}$ (Figure 5b). Overall, although the buoyancy conversion is stronger in August than that in March, the whole study region is predominantly characterized by positive b^1 values, indicating the conversion from submesoscale KE to SAPE.

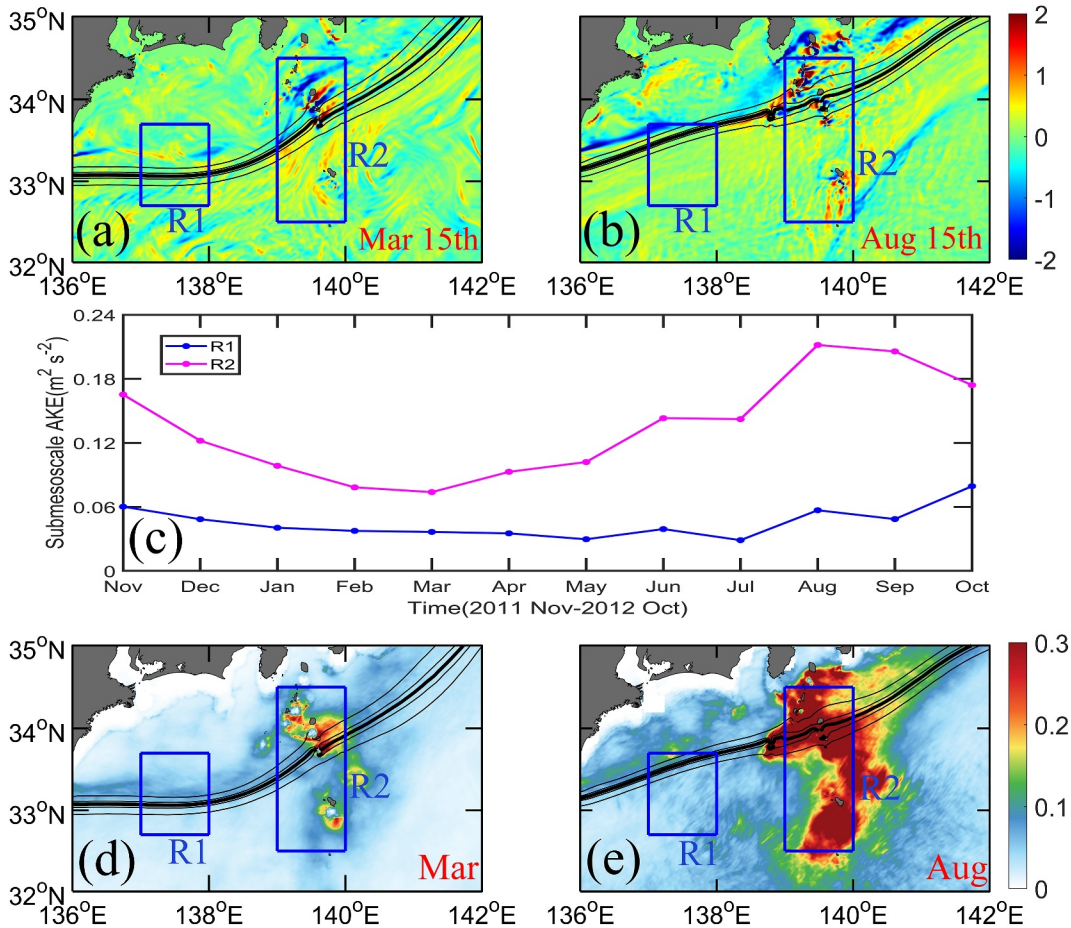

Figure 4. Snapshots of the Rossby number R_O at the sea surface for (a) 15 March and (b) 15 August (c): The time series of submesoscale ageostrophic kinetic energy (KE) (Submesoscale AKE, units: $m^2\ s^{-2}$), averaged over the upper 200 m in regions R1 (blue) and R2 (pink). (d) and (e) show the spatial distributions of monthly submesoscale ageostrophic KE for March and August, respectively (color shading, averaged over the upper 200 m, units: $m^2\ s^{-2}$). The blue boxes represent: region R1 (32.7°–33.7°N, 137°–138°E) and region R2 (32.5°–34.5°N, 139°–140°E), respectively. The monthly sea surface height (SSH) (contours, units: cm) for either March or August is superimposed, with thin black contours at 10 cm intervals between 60 and 90 cm, and the thick black contour indicates the main axis of the Kuroshio (defined by the 75-cm SSH contour).

In March, within the upper 200 m along Sections 1 and 2, the buoyancy conversion b^1 predominantly exhibits negative values, indicating that the conversion from SAPE to submesoscale KE dominates the study area. In Section 1, between 40 and 80 km, the negative b^1 reaches its minimum value of $-0.5 \times 10^{-6}\ m^2\ s^{-3}$; while positive values of b^1 reach up to $0.4 \times 10^{-6}\ m^2\ s^{-3}$, with a sparse distribution (Figure 6a). In Section 2, b^1 displays elevated values between 120 and 180 km, particularly near the islands, with peak magnitudes reaching $\pm 1.0 \times 10^{-6}\ m^2\ s^{-3}$ (Figure 6b). In August, both Section 1 and Section 2 exhibit strong positive values of b^1. In Section 1, b^1 reaches a maximum value of $1.0 \times 10^{-6}\ m^2\ s^{-3}$ between 30 and 40 km, at depths ranging from 30 to 90 m; but the negative b^1 is very weak (Figure 6c). As illustrated in Figure 6d, the extreme values of b^1 in Section 2 are markedly stronger than those in Section 1, attaining magnitudes of up to $\pm 1.0 \times 10^{-6}\ m^2\ s^{-3}$, with the most pronounced fluctuations clustered near the island region.

Overall, the above characteristics indicate the presence of a marked baroclinic instability process in the upper ocean, influenced by the Izu-Ogasawara Islands and accompanied by intense energy conversion between submesoscale KE and SAPE. In March, the conversion is primarily from SAPE to submesoscale KE, while in August, it predominantly occurs from submesoscale KE to SAPE, with a more intense conversion.

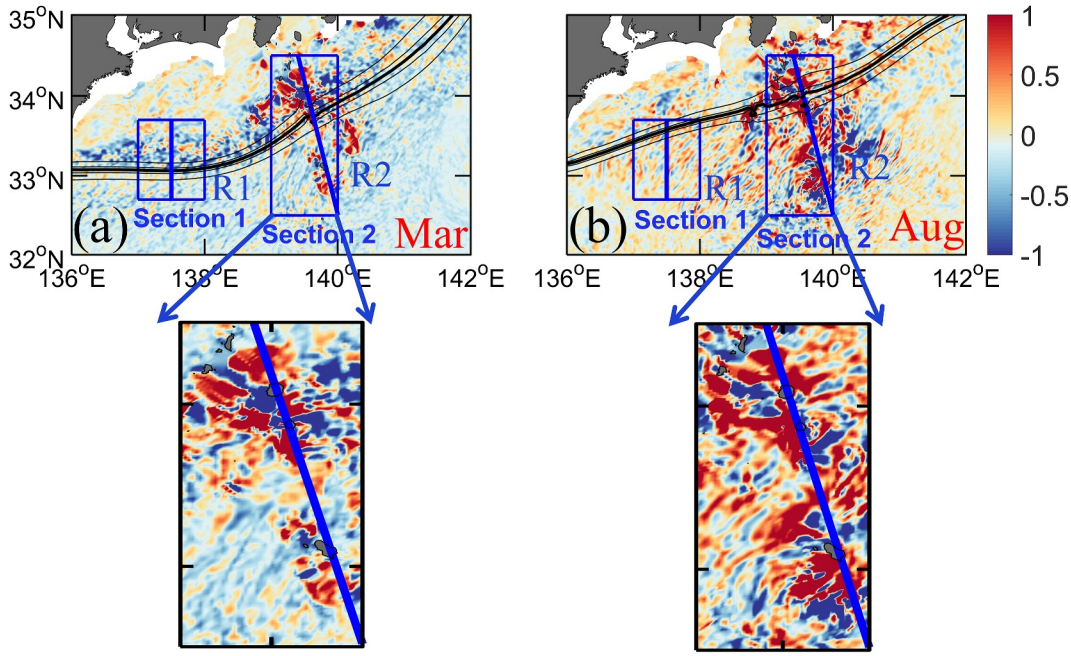

Figure 5. Distributions of the monthly buoyancy conversion b^1 (color shading, integrated over the upper 200 m, units: 10^{-4} m^3 s^{-3}) in March (a) and August (b). The monthly sea surface height (SSH) (contours, units: cm) for either March or August is superimposed, with thin black contours at 10 cm intervals between 60 and 90 cm, and the thick black contour indicates the main axis of the Kuroshio (defined by the 75-cm SSH contour). The blue boxes represent: region R1 (32.7°–33.7°N, 137°–138°E) and region R2 (32.5°–34.5°N, 139°–140°E), respectively. Section 1 (solid blue line) in region R1 is located at longitude 137.5°E, spanning from 32.7°N to 33.7°N. Section 2 (solid blue line) in region R2 is defined by the two endpoints: (140.0°E, 32.5°N) and (139.4°E, 34.5°N).

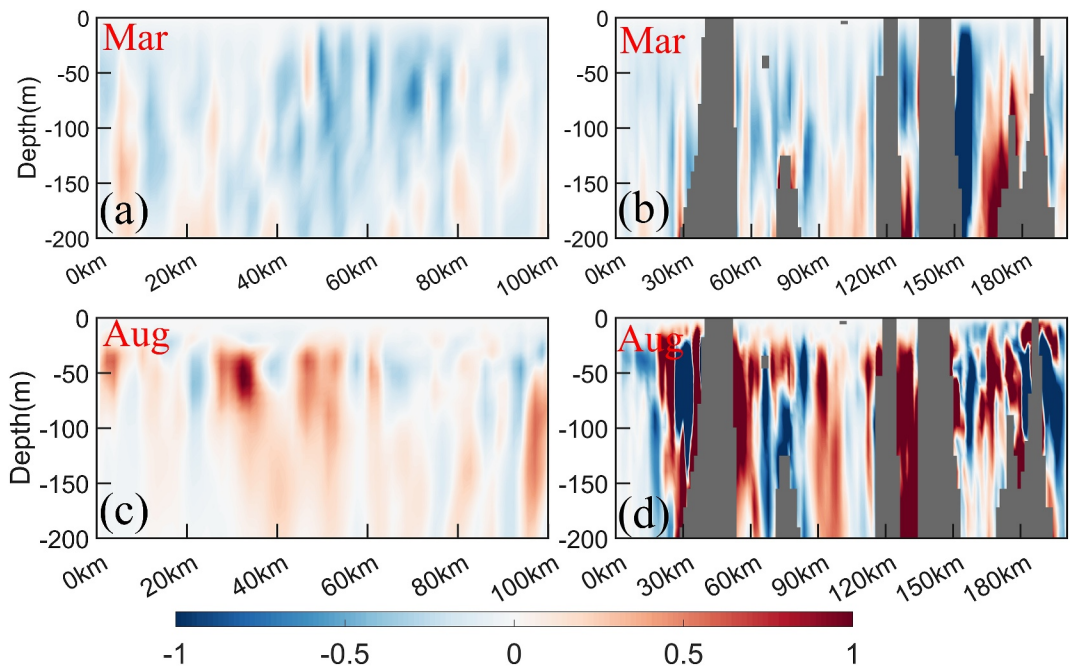

Figure 6. Sectional distributions of the monthly buoyancy conversion b^1 along Section 1 (left panels) and Section 2 (right panels) (color shading, units: 10^{-6} m^2 s^{-3}). Panels (a, b) correspond to March; panels (c, d) to August. Distance is measured from the minimum latitude—32.7°N in Section 1 and 32.5°N in section 2—and increases with latitude along each section.

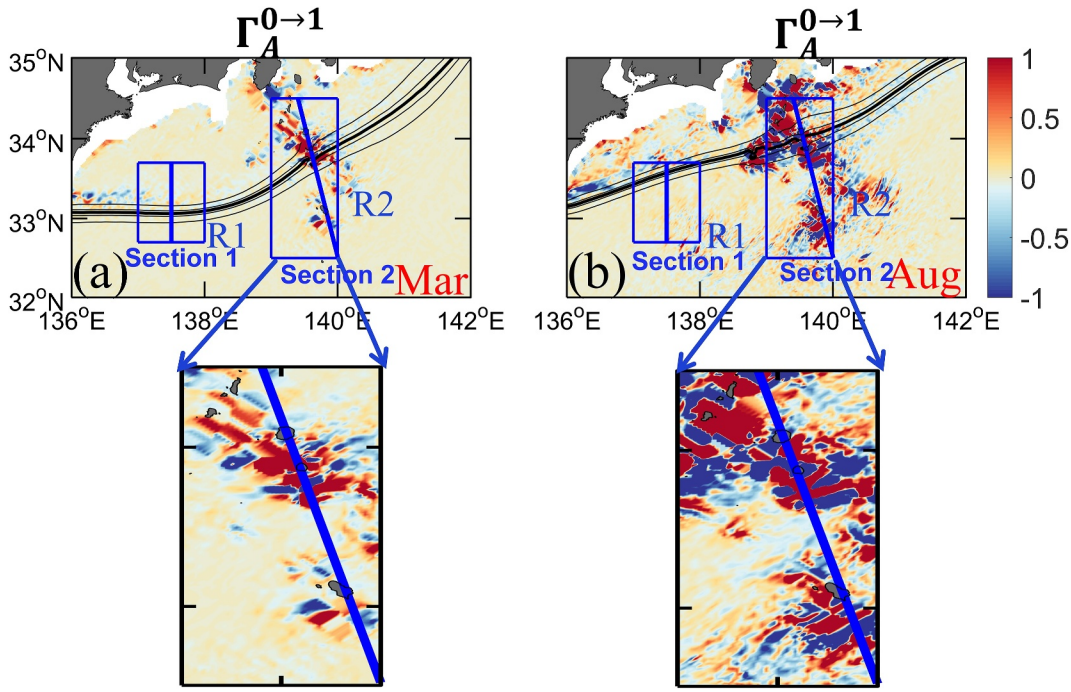

Figure 7. Distributions of the monthly ageostrophic kinetic energy transfer $\Gamma_A^{0\to1}$ (color shading, integrated over the upper 200 m, units: 10^{-3} m^3 s^{-3}) in March (a) and August (b). The monthly sea surface height (SSH) (contours, units: cm) for either March or August is superimposed, with thin black contours at 10 cm intervals between 60 and 90 cm, and the thick black contour indicates the main axis of the Kuroshio (defined by the 75-cm SSH contour). The blue boxes represent region R1 (32.7°–33.7°N, 137°–138°E) and region R2 (32.5°–34.5°N, 139°–140°E), respectively. Section 1 (solid blue line) in region R1 is located at longitude 137.5°E, spanning from 32.7°N to 33.7°N. Section 2 (solid blue line) in region R2 is defined by the two endpoints: (140.0°E, 32.5°N) and (139.4°E, 34.5°N).

4.2. Canonical Transfer

4.2.1. The Ageostrophic Kinetic Energy Transfer

The spatial distributions of ageostrophic KE transfer reveal significant ageostrophic motions in region R2, located around the Izu-Ogasawara Islands. In region R1, farther from the Izu-Ogasawara Islands, the ageostrophic KE transfer is weak. In March, high values of $\Gamma_A^{0\to1}$ are sparsely distributed around the northern side of the Izu-Ogasawara Islands (Figure 7a). The ageostrophic KE transfer is further enhanced in August. In August, the main axis of the Kuroshio crosses the Izu-Ogasawara Ridge along a path nearer to southern Japan. Strongly positive and negative values of $\Gamma_A^{0\to1}$ dominate the Izu-Ogasawara Islands region, revealing intense ageostrophic motions in this area. This facilitates efficient ageostrophic KE transfer between the background flow and the submesoscale windows. $\Gamma_A^{0\to1}$ exhibits a spatial pattern with alternating positive and negative values, reaching magnitudes of up to $\pm1.0 \times 10^{-3}$ m^3 s^{-3} (Figure 7b).

As shown in Figure 8, there is a strong ageostrophic KE cascade process in the upper ocean near the Izu-Ogasawara Islands while it is relatively weak in regions farther away. In March, no pronounced ageostrophic KE cascade is observed in Section 1 (Figure 8a). In Section 2, substantial $\Gamma_A^{0\to1}$ values are present near the islands. Specifically, between 120 and 160 km, at depths of 50–200 m, $\Gamma_A^{0\to1}$ predominantly exhibits significant positive values, with magnitudes reaching 8.0×10^{-6} m^2 s^{-3} (Figure 8b). In August, the magnitude of $\Gamma_A^{0\to1}$ is higher than that in March. In Section 1, a weak forward ageostrophic KE cascade occurs, with $\Gamma_A^{0\to1}$ reaching 4.0×10^{-6} m^2 s^{-3} (Figure 8c). In Section 2, marked ageostrophic KE transfer occurs across the island region. $\Gamma_A^{0\to1}$ is predominantly positive, reaching a maximum of 8.0×10^{-6} m^2 s^{-3}. Negative $\Gamma_A^{0\to1}$ values are prominently observed near the island region, with extreme values reaching -8.0×10^{-6} m^2 s^{-3} (Figure 8d).

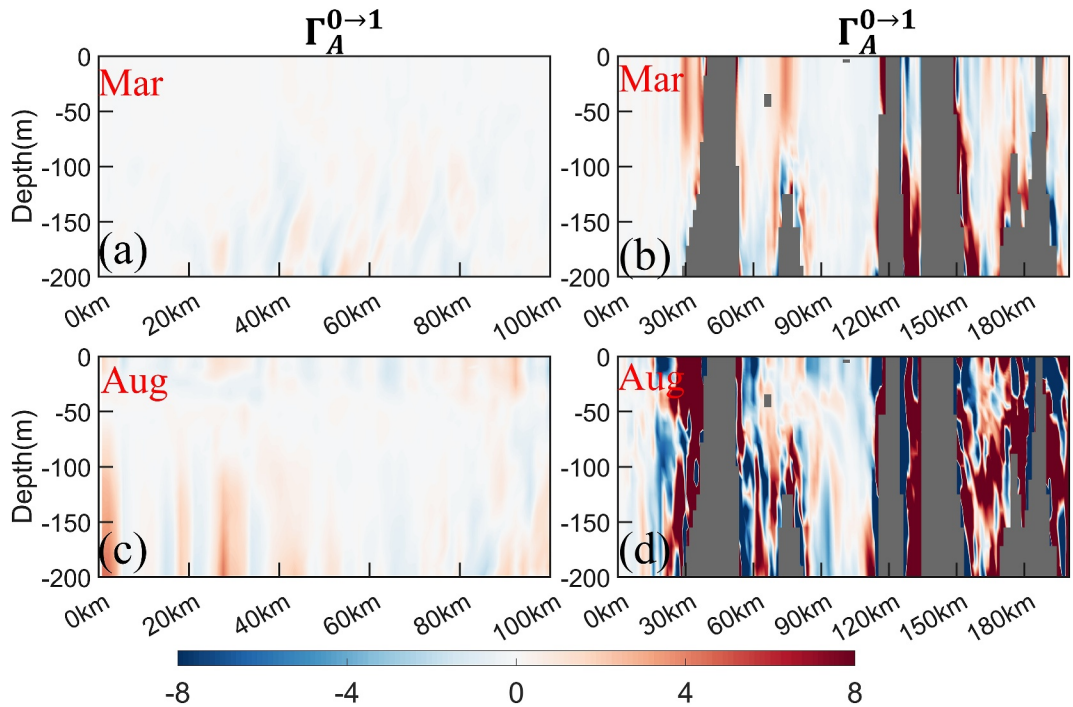

Figure 8. Sectional distributions of the monthly ageostrophic kinetic energy transfer $\Gamma_A^{0\to1}$ along Section 1 (left panels) and Section 2 (right panels) (color shading, units: 10^{-6} m^2 s^{-3}). Panels (a, b) correspond to March; panels (c, d) to August. Distance is measured from the minimum latitude—32.7°N in Section 1 and 32.5°N in section 2—and increases with latitude along each section.

4.2.2. Kinetic Energy Transfer Associated With Geostrophic-Ageostrophic Current Interactions

The Kuroshio, which primarily satisfies geostrophic balance, can be influenced by external forcing and other factors. These influences may disrupt the geostrophic balance and trigger interactions between geostrophic and ageostrophic flows. As shown in Figure 9, substantial KE transfer associated with geostrophic-ageostrophic current interactions $\Gamma_{GA}^{0\to1}$ is prominently distributed along the Izu-Ogasawara Islands, near region R2. Notably, $\Gamma_{GA}^{0\to1}$ exhibits a patchy distribution along the main axis of the Kuroshio. Therefore, a certain portion of $\Gamma_{GA}^{0\to1}$ also occurs near the main axis of the Kuroshio in region R1. $\Gamma_{GA}^{0\to1}$ in August is noticeably stronger than that in March. In March, the marked $\Gamma_{GA}^{0\to1}$ values are concentrated only along the northern side of the Izu-Ogasawara Islands (Figure 9a). In August, $\Gamma_{GA}^{0\to1}$ extends over most of the Izu-Ogasawara Island region, exhibiting a complex pattern of alternating positive and negative values (Figure 9b).

During March in Section 1, $\Gamma_{GA}^{0\to1}$ is predominantly positive but relatively weak, with an extremum of $\pm3.0 \times 10^{-6}$ m^2 s^{-3} (Figure 10a). In Section 2, intense $\Gamma_{GA}^{0\to1}$ values are primarily located around the islands. Between 120 and 150 km, at depths of 0–50 m, it is positive, with a maximum of 8.0×10^{-6} m^2 s^{-3}. In contrast, at depths of 50–200 m, $\Gamma_{GA}^{0\to1}$ becomes negative, reaching -8.0×10^{-6} m^2 s^{-3} (Figure 10b). The KE transfer, driven by the interactions between geostrophic and ageostrophic flows, is particularly pronounced in August. In Section 1, pronounced $\Gamma_{GA}^{0\to1}$ values are mainly concentrated between 60 and 100 km, predominantly within the upper 50 m layer, with positive values dominating and a peak magnitude of 8.0×10^{-6} m^2 s^{-3} (Figure 10c). In Section 2, near the islands, positive and negative values of $\Gamma_{GA}^{0\to1}$ alternate spatially, with both reaching extremes of $\pm8.0 \times 10^{-6}$ m^2 s^{-3} (Figure 10d).

4.3. Mean Energy Evolution Patterns

The mean energy evolution patterns and buoyancy conversion in regions R1 and R2 for March and August are shown in Table 2. In March and August, the submesoscale ageostrophic KE in region R1 is 0.04 m^2 s^{-2} and 0.06 m^2 s^{-2}, respectively, while in region R2, it is substantially higher at 0.07 m^2 s^{-2} and 0.21 m^2 s^{-2}. In March, the

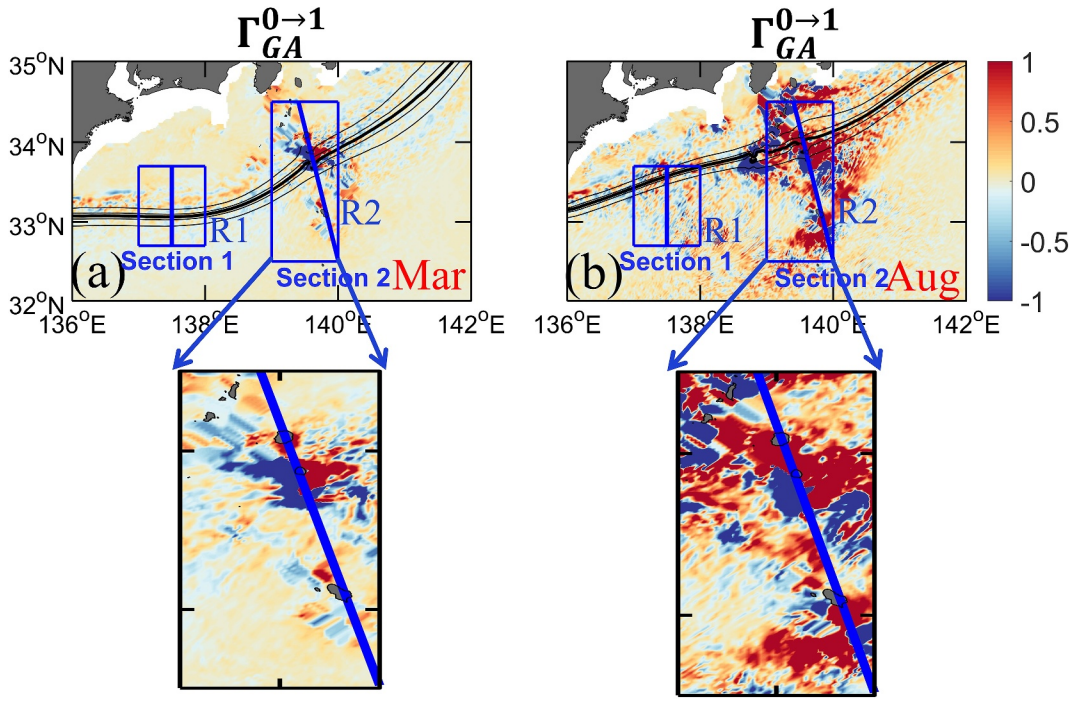

Figure 9. Similar to Figure 7, but for the kinetic energy transfer associated with geostrophic-ageostrophic current interactions $\Gamma_{GA}^{0\to1}$.

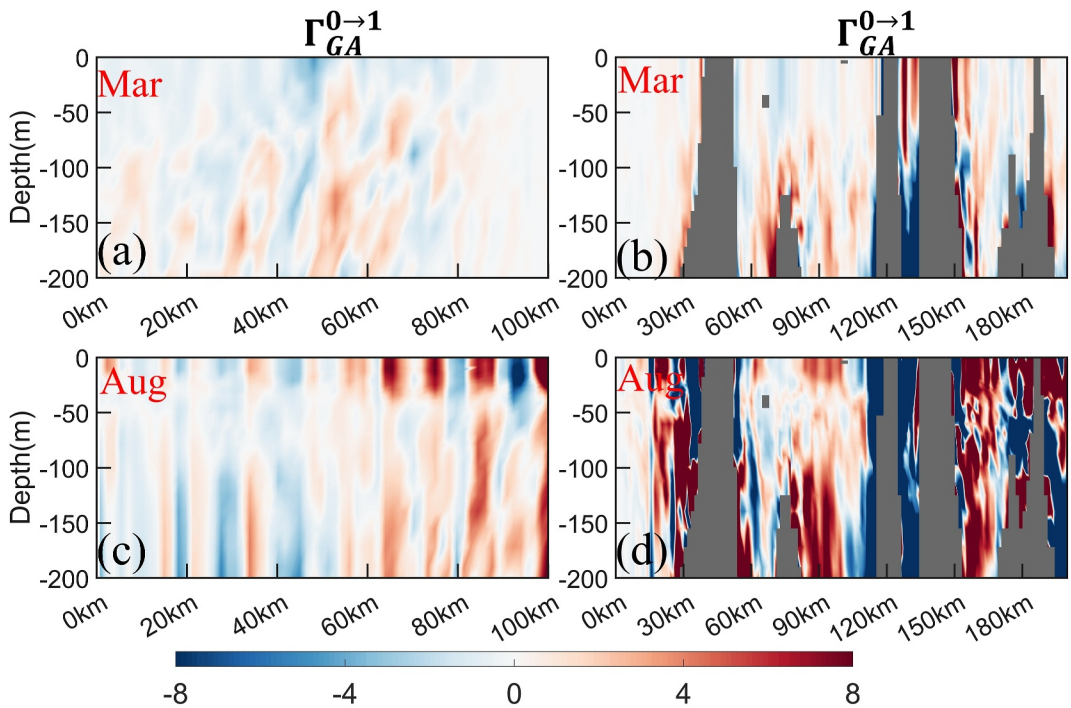

Figure 10. Similar to Figure 8, but for kinetic energy transfer associated with geostrophic-ageostrophic current interactions $\Gamma_{GA}^{0\to1}$.

Table 2
Monthly Mean Energy Evolution Patterns in Regions R1 and R2

Terms / Region	Time	Sub-AKE	b^1	$\Gamma^{0\to1}$	$\Gamma_G^{0\to1}$	$\Gamma_A^{0\to1}$	$\Gamma_{GA}^{0\to1}$
R1	March	0.04	−1.80	−2.18	−1.34	−0.46	−0.38
	August	0.06	0.04	−2.98	−2.10	−0.58	−0.30
R2	March	0.07	−1.09	−7.36	−17.22	5.45	4.41
	August	0.21	1.71	−3.95	−19.43	6.30	9.18

Note. Sub-AKE represents submesoscale ageostrophic KE (averaged over the upper ocean, 0–200 m, units: $m^2\ s^{-2}$). The KE transfers are represented by $\Gamma^{0\to1}$, $\Gamma_G^{0\to1}$, $\Gamma_A^{0\to1}$, $\Gamma_{GA}^{0\to1}$, and buoyancy conversion b^1 (integrated over the upper ocean, 0–200 m, units: $10^{-5}\ m^3\ s^{-3}$).

buoyancy conversion is negative in regions R1 and R2, indicating a transfer of SAPE to submesoscale KE. Especially in region R1, it reaches $-1.80 \times 10^{-5}\ m^3\ s^{-3}$, serving as the primary source of submesoscale KE in this region. Although the buoyancy conversion in region R2 reaches $-1.09 \times 10^{-5}\ m^3\ s^{-3}$, the contribution of SAPE is comparatively weak relative to the forward cascade of KE from the background flow.

As an ocean circulation, the Kuroshio's KE is primarily stored as geostrophic KE, exhibiting notable geostrophic KE transfer between the background flow and submesoscale windows. In regions R1 and R2, geostrophic KE mainly transfers in an inverse cascade from the submesoscale window back to the background flow window. In contrast, the ageostrophic KE in region R2 presents a significant forward cascade between the background flow and submesoscale windows, reaching as high as $6.30 \times 10^{-5}\ m^3\ s^{-3}$ in August. In region R1, the ageostrophic KE presents an inverse cascade between the background flow and submesoscale windows during both March and August.

Notably, submesoscale motions are characterized by a combination of geostrophic and ageostrophic components and based on the decomposition results of MWT, the KE on the submesoscale window is primarily composed of ageostrophic KE. So, we consider the KE transfer associated with geostrophic-ageostrophic current interactions as another source of submesoscale ageostrophic KE in the study region. In region R1, the KE transfer induced by interactions between geostrophic and ageostrophic current predominantly exhibits an inverse cascade from the submesoscale to the background flow windows. In region R2, this energy primarily cascades from the background flow to the submesoscale windows, with the most substantial contributions occurring in August, when forward cascade values of $\Gamma_{GA}^{0\to1}$ reach up to $9.18 \times 10^{-5}\ m^3\ s^{-3}$.

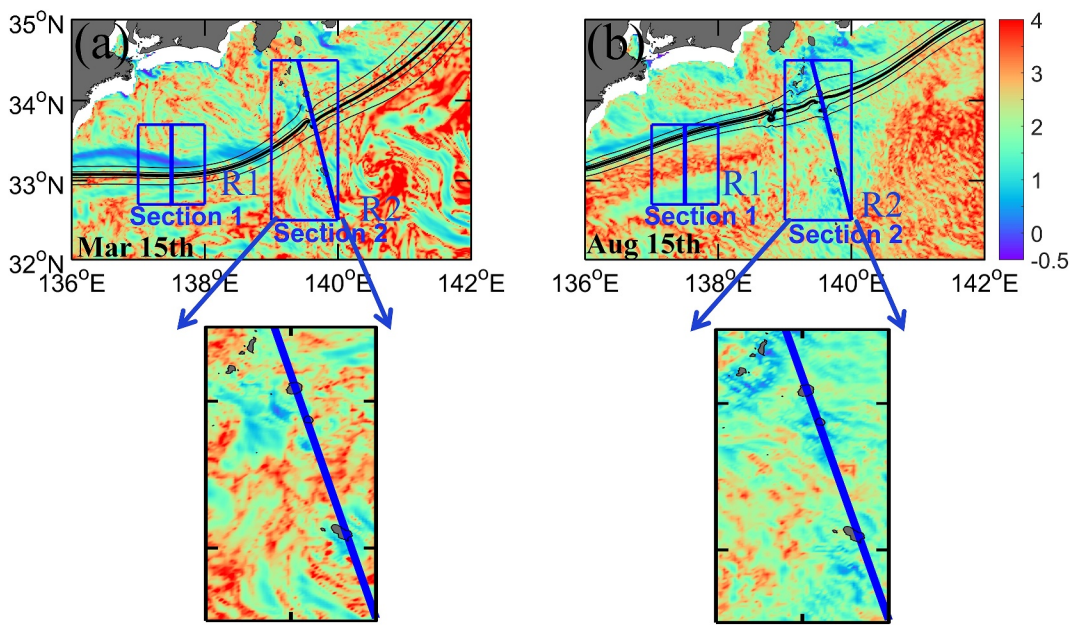

Figure 11. Logarithm (base 10) of the geostrophic Richardson number R_{ig} averaged over the upper 200 m, for (a) 15 March and (b) 15 August with the monthly sea surface height (SSH) superimposed (contours, units: cm). The thin black contours represent 60–90 cm with an interval of 10 cm, and the thick black contour indicates the main axis of the Kuroshio (defined by the 75-cm SSH contour). The blue boxes represent region R1 (32.7°–33.7°N, 137°–138°E) and region R2 (32.5°–34.5°N, 139°–140°E), respectively. Section 1 (solid blue line) in region R1 is located at longitude 137.5°E, spanning from 32.7°N to 33.7°N. Section 2 (solid blue line) in region R2 is defined by the two endpoints: (140.0°E, 32.5°N) and (139.4°E, 34.5°N).

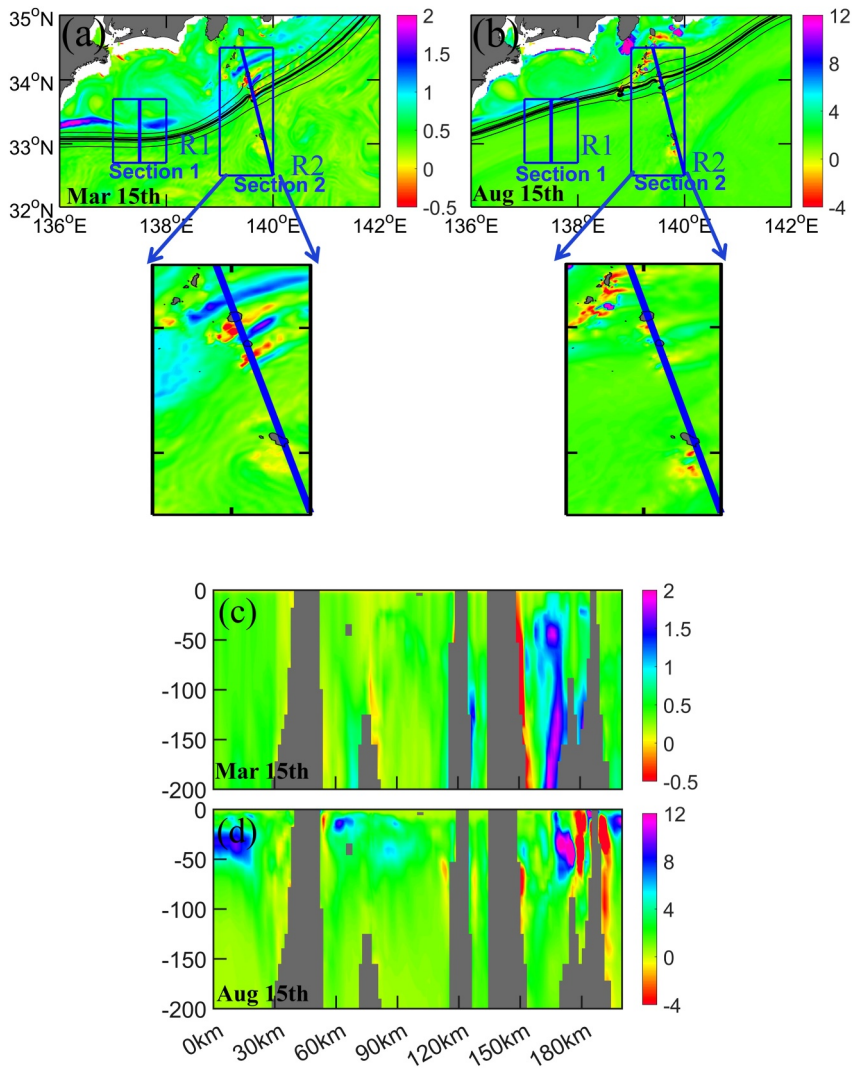

Figure 12. Snapshots of Ertel potential vorticity (PV) (color shading, units: $\times 10^{-8} s^{-3}$) averaged over the upper 200 m, for (a) 15 March and (b) 15 August. The blue boxes represent: region R1 (32.7°–33.7°N, 137°–138°E) and region R2 (32.5°–34.5°N, 139°–140°E), respectively. The monthly sea surface height (SSH) (contours, units: cm) for either March or August is superimposed, with thin black contours at 10 cm intervals between 60 and 90 cm, and the thick black contour indicating the main axis of the Kuroshio (defined by the 75-cm SSH contour). Section 1 (solid blue line) in region R1 is located at longitude 137.5°E, spanning from 32.7°N to 33.7°N. Section 2 (solid blue line) in region R2 is defined by the two endpoints: (140.0°E, 32.5°N) and (139.4°E, 34.5°N). Sectional distributions of Ertel PV along Section 2 (color shading, units: $\times 10^{-8} s^{-3}$) for (c) 15 March and (d) 15 August. Distance is measured from the location of minimum latitude (32.5°N), increasing with latitude along Section 2.

5. Ageostrophic Centrifugal Instability

Figure 11 shows the distributions of the logarithm of the geostrophic Richardson number (R_{ig}) averaged over the upper 200 m for 15 March and 15 August. Across the study region, high values of the R_{ig} are prevalent, whereas relatively low R_{ig} values are observed near the main axis of the Kuroshio and in the vicinity of the Izu-Ogasawara Islands. On 15 March, low R_{ig} values are clearly observed along the Kuroshio axis between 136°E and 138°E, and in region R2 near the Izu-Ogasawara Islands. Compared with 15 March, 15 August shows less pronounced low R_{ig} values along the Kuroshio axis between 136°E and 138°E, although region R2 still maintains relatively low values (Figure 11b). Low R_{ig} provides a favorable condition for submesoscale phenomena and may trigger various instability mechanisms (Hoskins, 1974; Thomas et al., 2013).

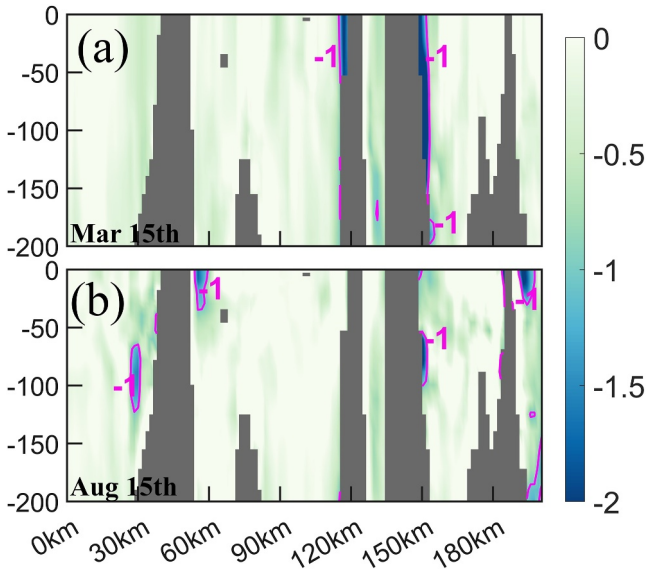

Figure 13. Sectional distributions of Rossby number R_O along Section 2 for (a) 15 March and (b) 15 August. Distance is measured from the location of minimum latitude (32.5°N), increasing with latitude along Section 2. The pink contour lines correspond to $R_O = -1$.

As illustrated in Figures 12a and 12b, Ertel PV in the study region is predominantly positive, whereas negative Ertel PV values are found near the Izu-Ogasawara Islands. On 15 March, the sectional distributions of Ertel PV in region R2 further reveal that notable negative values appear near 150 km, in the vicinity of the Izu-Ogasawara Islands, extending throughout the entire 0–200 m depth range (Figure 12c). On 15 August, pronounced negative Ertel PV values are observed around 180 km near the Izu-Ogasawara Islands at depths of 0–100 m (Figure 12d). A change in the sign of Ertel PV constitutes a sufficient condition for the development of instability. The fluid becomes unstable and the relative vorticity ζ falls below $-f$, leading to the development of ageostrophic centrifugal instability (CI; Gula et al., 2016; Hoskins, 1974; Thomas et al., 2013). Under such conditions, the influence of ageostrophic motions becomes significant. The presence of $R_O < -1$ near the Izu-Ogasawara Islands further indicates the occurrence of ageostrophic CI (Figures 13a and 13b).

6. Discussion

According to the MWT analysis, pronounced ageostrophic KE is observed on the submesoscale window in the Kuroshio south of Japan, with elevated values concentrated around the Izu-Ogasawara Islands (region R2).

In region R2, the submesoscale ageostrophic KE exhibits a seasonal variation, being weaker in winter and stronger in summer. The submesoscale ageostrophic KE reaches its minimum in March and its maximum in August. Furthermore, the KE cascade process is more intense in August compared with March. The Kuroshio displays significant seasonal variations, characterized by higher volume transport and stronger KE in summer and autumn, but lower volume transport and weaker KE in winter and spring (Kagimoto & Yamagata, 1997; Sekine & Kutsuwada, 1994). As shown in Figure 14, in region R2, both the background geostrophic and ageostrophic KE exhibit seasonal variation patterns consistent with those of the submesoscale ageostrophic KE. In region R2, the higher background geostrophic and ageostrophic KEs during the summer provide energy sources for the generation of submesoscale ageostrophic KE. Previous studies showed that the Izu-Ogasawara Ridge forms a deep-water channel near 34°N, with a shallow ridge structure extending to the south. When the Kuroshio flows near 34°N, south of Japan, it follows a nearshore path. Conversely, when it flows farther from 34°N, it is regarded as an offshore path (Hurlburt et al., 1996; Sugimoto & Hanawa, 2012). When the Kuroshio crosses over the Izu-Ogasawara Ridge along a nearshore path, it tends to become more unstable, with energy more readily dissipating toward smaller scales (Yang & Liang, 2019;

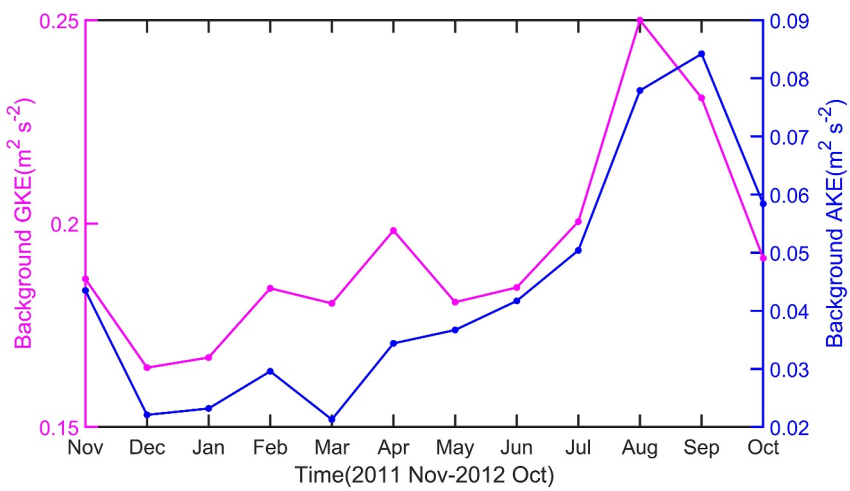

Figure 14. Mean background geostrophic kinetic energy (KE) (Background GKE, pink, units: m^2 s^{-2}) and ageostrophic KE (Background AKE, blue, units: m^2 s^{-2}) in region R2.

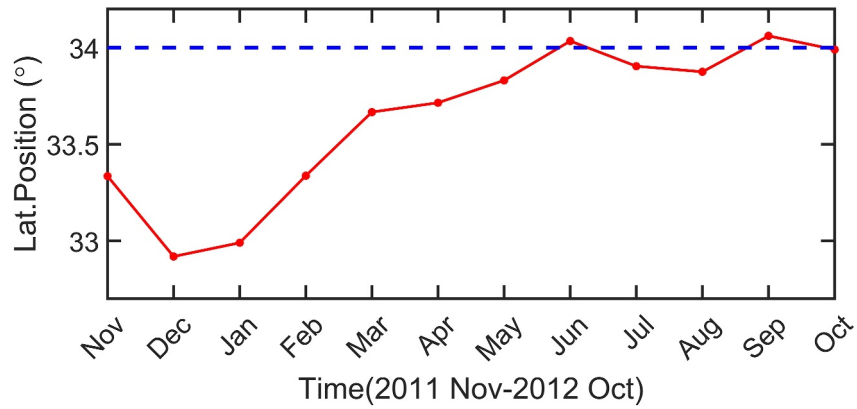

Figure 15. Mean latitude for the main axis of the Kuroshio (defined by the 75-cm sea surface height contour) in the south of Japan, between 136°E and 141°E. The blue dashed line indicates the 34°N latitude.

Yasuda et al., 1985). As shown in Figure 15, from summer to autumn, the Kuroshio south of Japan follows a relatively nearshore path as it crosses over the Izu-Ogasawara Ridge.

As shown in Figures 11–13, prominent ageostrophic CI occurs around the island region over the Izu-Ogasawara Ridge, with slightly stronger intensity in August compared with March. Ageostrophic CI can extract KE from larger-scale balanced currents and enhance the forward cascade of KE (Gula et al., 2016; Thomas et al., 2013). In addition, ageostrophic CI is also intensified in topographic wakes (Dewar et al., 2015; Molemaker et al., 2015). Therefore, in August, the Kuroshio follows a nearshore path and crosses the Izu-Ogasawara Islands. During this period, the background KE is relatively high. Significant ageostrophic CI is associated with ageostrophic motions and interactions between geostrophic and ageostrophic flows. Their synergistic effects trigger a series of intense forward KE cascades, resulting in the most prominent submesoscale ageostrophic KE being observed. In March, as the Kuroshio passes the Izu-Ogasawara Islands, it follows a more offshore path. The background KE is weaker, and ageostrophic CI is less pronounced, leading to less submesoscale ageostrophic KE.

7. Conclusions

This study utilizes the MITgcm LLC-4320 simulation, with a resolution of 1/48°, to investigate the temporal and spatial variability of submesoscale KE in the Kuroshio south of Japan, as well as the mechanisms driving this variability. We employ a developed functional analysis tool, MWT, and the MWT-based theory of canonical transfer. Using the MWT, the total, geostrophic, and ageostrophic velocities in the study region are decomposed into two temporal windows: the background flow window and the submesoscale window. Based on canonical transfer theory, we quantitatively evaluate the contributions of cross-scale KE transfer and the conversion of SAPE to submesoscale KE. The submesoscale window is dominated by ageostrophic KE, with notable submesoscale ageostrophic KE mainly distributed near the island region over the Izu-Ogasawara Ridge. This KE reaches its minimum in March and peaks in August, exhibiting a distinct seasonal variation.

In August, the Kuroshio follows a nearshore path, accompanied by high background geostrophic and ageostrophic KE, as it flows along the Izu-Ogasawara Islands. As the Kuroshio interacts with the islands, the disruption of geostrophic balance leads to the development of ageostrophic CI. This instability is closely linked to ageostrophic motions and enhances interactions between geostrophic and ageostrophic flows. These processes facilitate intense ageostrophic KE transfer, as well as KE transfer associated with geostrophic-ageostrophic current interactions, from the background flow window to the submesoscale window. As a result, they constitute the primary source of the pronounced submesoscale ageostrophic KE in this region, with both types of KE transfers contributing comparably to the generation of this ageostrophic KE. The conversion from SAPE to submesoscale KE is not significant in this region.

In March, the Kuroshio follows an offshore path, with relatively low background geostrophic and ageostrophic KE as it passes over the Izu-Ogasawara Islands, accompanied by a relatively weak ageostrophic CI. This generates a subdued forward energy cascade involving both ageostrophic motions and geostrophic-ageostrophic

interactions, resulting in weak submesoscale ageostrophic KE compared with August. Similarly, the conversion from SAPE to submesoscale KE is not pronounced.

However, there is no significant submesoscale ageostrophic KE in regions farther from the islands; its seasonal variability is weak, and no evident signatures of ageostrophic CI are identified. Meanwhile, a weak inverse cascade involving both ageostrophic motions and their interactions with geostrophic flow transfers KE from the submesoscale ageostrophic KE reservoir back to the background flow window. In March, the conversion from SAPE to submesoscale KE is the dominant source of submesoscale KE in this region, whereas in August, the effect of this conversion is not significant.

Conflict of Interest

The authors declare no conflicts of interest relevant to this study.

Data Availability Statement

The LLC-4320 data set is available at https://data.nas.nasa.gov/ecco, and the ETOPO 2022 15-Arc-Second Global Relief Model (NOAA National Centers for Environmental Information, 2022) can be accessed via https://doi.org/10.25921/fd45-gt74. The MWT software can be downloaded from http://www.ncoads.org/.

Acknowledgments
This work is supported by the National Natural Science Foundation of China (Grant 92158201, 42376001, 42276017, and 42230105) and the Fundamental Research Funds for the Central Universities (Grant 20720240104).

References

Abarbanel, H. D. I., Holm, D. D., Marsden, J. E., & Ratiu, T. (1984). Richardson number criterion for the nonlinear stability of three-dimensional stratified flow. *Physical Review Letters*, *52*(26), 2352–2355. https://doi.org/10.1103/PhysRevLett.52.2352

Arbic, B. K., Scott, R. B., Flierl, G. R., Morten, A. J., Richman, J. G., & Shriver, J. F. (2012). Nonlinear cascades of surface oceanic geostrophic kinetic energy in the frequency domain. *Journal of Physical Oceanography*, *42*(9), 1577–1600. https://doi.org/10.1175/JPO-D-11-0151.1

Capet, X., McWilliams, J. C., Molemaker, M. J., & Shchepetkin, A. F. (2008). Mesoscale to submesoscale transition in the California current system. Part I: Flow structure, eddy flux, and observational tests. *Journal of Physical Oceanography*, *38*(1), 29–43. https://doi.org/10.1175/2007JPO3671.1

Chen, J., Zhu, X. H., Nakamura, H., Zhao, R., Wang, M., Zheng, H., & Nishina, A. (2024). Submesoscale processes fueled by the Kuroshio in the Tokara Strait. *Journal of Geophysical Research: Oceans*, *129*(3), e2022JC019561. https://doi.org/10.1029/2022JC019561

D'Asaro, E., Lee, C., Rainville, L., Harcourt, R., & Thomas, L. (2011). Enhanced turbulence and energy dissipation at ocean fronts. *Science*, *332*(6027), 318–322. https://doi.org/10.1126/science.1201515

Dewar, W. K., McWilliams, J. C., & Molemaker, M. J. (2015). Centrifugal instability and mixing in the California undercurrent. *Journal of Physical Oceanography*, *45*(5), 1224–1241. https://doi.org/10.1175/JPO-D-13-0269.1

Dong, C. M., McWilliams, J. C., & Shchepetkin, A. F. (2007). Island wakes in deep water. *Journal of Physical Oceanography*, *37*(4), 962–981. https://doi.org/10.1175/JPO3047.1

Ferrari, R., & Wunsch, C. (2009). Ocean circulation kinetic energy: Reservoirs, sources, and sinks. *Annual Review of Fluid Mechanics*, *41*(1), 253–282. https://doi.org/10.1146/annurev.fluid.40.111406.102139

Galperin, B., Sukoriansky, S., & Anderson, P. S. (2007). On the critical Richardson number in stably stratified turbulence. *Atmospheric Science Letters*, *8*(3), 65–69. https://doi.org/10.1002/asl.153

Grooms, I. (2015). Submesoscale baroclinic instability in the balance equations. *Journal of Fluid Mechanics*, *762*, 256–272. https://doi.org/10.1017/jfm.2014.657

Gula, J., Molemaker, M. J., & McWilliams, J. C. (2015). Topographic vorticity generation, submesoscale instability and vortex street formation in the Gulf Stream. *Geophysical Research Letters*, *42*(10), 4054–4062. https://doi.org/10.1002/2015GL063731

Gula, J., Molemaker, M. J., & McWilliams, J. C. (2016). Topographic generation of submesoscale centrifugal instability and energy dissipation. *Nature Communications*, *7*(1), 12811. https://doi.org/10.1038/ncomms12811

Hasegawa, D., Yamazaki, H., Lueck, R. G., & Seuront, L. (2004). How islands stir and fertilize the upper ocean. *Geophysical Research Letters*, *31*(16), L16303. https://doi.org/10.1029/2004GL020143

Hoskins, B. J. (1974). The role of potential vorticity in symmetric stability and instability. *Quarterly Journal of the Royal Meteorological Society*, *100*(425), 480–482. https://doi.org/10.1002/qj.49710042520

Hurlburt, H. E., Wallcraft, A. J., Schmitz Jr, W. J., Hogan, P. J., & Metzger, E. J. (1996). Dynamics of the Kuroshio/Oyashio current system using eddy-resolving models of the North Pacific Ocean. *Journal of Geophysical Research*, *101*(C1), 941–976. https://doi.org/10.1029/95JC01674

Jing, Z. Y., Fox-Kemper, B., Cao, H. J., Zheng, R. X., & Du, Y. (2021). Submesoscale fronts and their dynamical processes associated with symmetric instability in the Northwest Pacific subtropical ocean. *Journal of Physical Oceanography*, *51*(1), 83–100. https://doi.org/10.1175/JPO-D-20-0076.1

Kagimoto, T., & Yamagata, T. (1997). Seasonal transport variations of the Kuroshio: An OGCM simulation. *Journal of Physical Oceanography*, *27*(3), 403–418. https://doi.org/10.1175/1520-0485(1997)027<0403:STVOTK>2.0.CO;2

Liang, X. S. (2016). Canonical transfer and multiscale energetics for primitive and quasi-geostrophic atmospheres. *Journal of the Atmospheric Sciences*, *73*(11), 4439–4468. https://doi.org/10.1175/JAS-D-16-0131.1

Liang, X. S., & Anderson, D. G. M. (2007). Multiscale window transform. *Multiscale Modeling and Simulation*, *6*(2), 437–467. https://doi.org/10.1137/06066895X

Liang, X. S., & Robinson, A. R. (2007). Localized multi-scale energy and vorticity analysis: II. Finite-amplitude instability theory and validation. *Dynamics of Atmospheres and Oceans*, *44*(2), 51–76. https://doi.org/10.1016/j.dynatmoce.2007.04.001

Mahadevan, A., & Tandon, A. (2006). An analysis of mechanisms for submesoscale vertical motion at ocean fronts. *Ocean Modelling*, *14*(3–4), 241–256. https://doi.org/10.1016/j.ocemod.2006.05.006

Masunaga, E., Uchiyama, Y., Zhang, X., Kimura, W., & Kosako, T. (2022). Modulation of submesoscale motions due to tides and a shallow ridge along the Kuroshio. *Deep Sea Research Part I: Oceanographic Research Papers*, *186*, 103828. https://doi.org/10.1016/j.dsr.2022.103828

McWilliams, J. C. (2016). Submesoscale currents in the ocean. *Proceedings of the Royal Society A: Mathematical, Physical and Engineering Sciences*, *472*(2189), 20160117. https://doi.org/10.1098/rspa.2016.0117

McWilliams, J. C. (2017). Submesoscale surface fronts and filaments: Secondary circulation, buoyancy flux, and frontogenesis. *Journal of Fluid Mechanics*, *823*, 391–432. https://doi.org/10.1017/jfm.2017.294

McWilliams, J. C. (2019). A survey of submesoscale currents. *Geoscience Letters*, *6*(1), 3. https://doi.org/10.1186/s40562-019-0133-3

Molemaker, M. J., McWilliams, J. C., & Dewar, W. K. (2015). Submesoscale instability and generation of mesoscale anticyclones near a separation of the California undercurrent. *Journal of Physical Oceanography*, *45*(3), 613–629. https://doi.org/10.1175/JPO-D-13-0225.1

Mulet, S., Rio, M. H., Mignot, A., Guinehut, S., & Morrow, R. (2012). A new estimate of the global 3D geostrophic ocean circulation based on satellite data and in-situ measurements. *Deep Sea Research Part II: Topical Studies in Oceanography*, *77*, 70–81. https://doi.org/10.1016/j.dsr2.2012.04.012

Nagai, T., Hasegawa, D., Tanaka, T., Nakamura, H., Tsutsumi, E., Inoue, R., & Yamashiro, T. (2017). First evidence of coherent bands of strong turbulent layers associated with high-wavenumber internal-wave shear in the upstream Kuroshio. *Scientific Reports*, *7*(1), 14555. https://doi.org/10.1038/s41598-017-15167-1

Napolitano, D. C., da Silveira, I. C. A., Tandon, A., & Calil, P. H. R. (2020). Submesoscale phenomena due to the Brazil current crossing of the Vitória-Trindade Ridge. *Journal of Geophysical Research: Oceans*, *125*, e2020JC016731. https://doi.org/10.1029/2020JC016731

Naveira Garabato, A. C., Frajka-Williams, E. E., Spingys, Legg, S., Polzin, K. L., Forryan, A., et al., (2019). Rapid mixing and exchange of deep-ocean waters in an abyssal boundary current. *Proceedings of the National Academy of Sciences*, *116*(27), 1323–13238. https://doi.org/10.1073/pnas.1904087116

NOAA National Centers for Environmental Information. (2022). *ETOPO 2022 15 arc-second global relief model*. NOAA National Centers for Environmental Information. https://doi.org/10.25921/fd45-gt74

Perfect, B., Kumar, N., & Riley, J. J. (2018). Vortex structures in the wake of an idealized seamount in rotating, stratified flow. *Geophysical Research Letters*, *45*(17), 9098–9105. https://doi.org/10.1029/2018GL078703

Qiu, B., Nakano, T., Chen, S., & Klein, P. (2017). Submesoscale transition from geostrophic flows to internal waves in the northwestern Pacific upper ocean. *Nature Communications*, *8*(1), 14055. https://doi.org/10.1038/ncomms14055

Qiu, C., Yang, Z., Wang, D., Feng, M., & Su, J. (2022). The enhancement of submesoscale ageostrophic motion on the mesoscale eddies in the South China Sea. *Journal of Geophysical Research: Oceans*, *127*(9), e2022JC018736. https://doi.org/10.1029/2022JC018736

Ruan, X., Thompson, A. F., Flexas, M. M., & Sprintall, J. (2017). Contribution of topographically generated submesoscale turbulence to Southern Ocean overturning. *Nature Geoscience*, *10*(11), 840–845. https://doi.org/10.1038/ngeo3053

Sekine, Y. (1990). A numerical experiment on the path dynamics of the Kuroshio with reference to the formation of the large meander path south of Japan. *Deep-Sea Research, Part A: Oceanographic Research Papers*, *37*(3), 359–380. https://doi.org/10.1016/0198-0149(90)90014-M

Sekine, Y., & Kutsuwada, K. (1994). Seasonal variation in volume transport of the Kuroshio south of Japan. *Journal of Physical Oceanography*, *24*(2), 261–272. https://doi.org/10.1175/1520-0485(1994)024<0261:SVIVTO>2.0.CO;2

Sekine, Y., & Toba, Y. (1981). Velocity variation of the Kuroshio during formation of the small meander south of Kyûshû. *Journal of the Oceanographical Society of Japan*, *37*(2), 87–93. https://doi.org/10.1007/BF02072561

Soeyanto, E., Guo, X., Ono, J., & Miyazawa, Y. (2014). Interannual variations of Kuroshio transport in the East China Sea and its relation to the Pacific decadal oscillation and mesoscale eddies. *Journal of Geophysical Research: Oceans*, *119*(6), 3595–3616. https://doi.org/10.1002/2013JC009529

Srinivasan, K., McWilliams, J. C., Molemaker, M. J., & Barkan, R. (2019). Submesoscale vortical wakes in the lee of topography. *Journal of Physical Oceanography*, *49*(7), 1949–1971. https://doi.org/10.1175/JPO-D-18-0042.1

Srinivasan, K., McWilliams, J. C., Renault, L., Hristova, H. G., Molemaker, J., & Kessler, W. S. (2017). Topographic and mixed layer submesoscale currents in the near-surface southwestern tropical Pacific. *Journal of Physical Oceanography*, *47*(6), 1221–1242. https://doi.org/10.1175/JPO-D-16-0216.1

Stone, P. H. (1966). On non-geostrophic baroclinic stability. *Journal of the Atmospheric Sciences*, *23*(4), 390–400. https://doi.org/10.1175/1520-0469(1966)023<0390:ONGBS>2.0.CO;2

Stone, P. H. (1970). On non-geostrophic baroclinic stability: Part II. *Journal of the Atmospheric Sciences*, *27*(5), 721–726. https://doi.org/10.1175/1520-0469(1970)027<0721:ONGBSP>2.0.CO;2

Su, Z., Wang, J., Klein, P., Thompson, A. F., & Menemenlis, D. (2018). Ocean submesoscales as a key component of the global heat budget. *Nature Communications*, *9*(1), 775. https://doi.org/10.1038/s41467-018-02983-w

Sugimoto, S., & Hanawa, K. (2012). Relationship between the path of the Kuroshio in the south of Japan and the path of the Kuroshio extension in the east. *Journal of Oceanography*, *68*(1), 219–225. https://doi.org/10.1007/s10872-011-0089-1

Thomas, L. N. (2008). Formation of intrathermocline eddies at ocean fronts by wind-driven destruction of potential vorticity. *Dynamics of Atmospheres and Oceans*, *45*(3–4), 252–273. https://doi.org/10.1016/j.dynatmoce.2008.02.002

Thomas, L. N., Tandon, A., & Mahadevan, A. (2008). Submesoscale processes and dynamics. In M. W. Hecht & H. Hasumi (Eds.), *Ocean modeling in an eddying regime, geophysical monograph series* (Vol. 177, pp. 17–38). American Geophysical Union. Washington, DC. https://doi.org/10.1029/177GM04

Thomas, L. N., Taylor, J. R., Ferrari, R., & Joyce, T. M. (2013). Symmetric instability in the Gulf Stream. *Deep Sea Research Part II: Topical Studies in Oceanography*, *91*, 96–110. https://doi.org/10.1016/j.dsr2.2013.02.025

Tsutsumi, E., Matsuno, T., Lien, R.-C., Nakamura, H., Senjyu, T., & Guo, X. (2017). Turbulent mixing within the Kuroshio in the Tokara Strait. *Journal of Geophysical Research: Oceans*, *122*(9), 7082–7094. https://doi.org/10.1002/2017JC013049

Wang, Y. L., Wu, C. R., & Chao, S. Y. (2016). Warming and weakening trends of the Kuroshio during 1993-2013. *Geophysical Research Letters*, *43*(17), 9200–9207. https://doi.org/10.1002/2016GL069432

Yang, Y., & Liang, X. S. (2019). New perspectives on the generation and maintenance of the Kuroshio large meander. *Journal of Physical Oceanography*, *49*(8), 2095–2113. https://doi.org/10.1175/JPO-D-18-0276.1

Yang, Y., Liang, X. S., & He, W. B. (2024). On the formation and maintenance of the interannual variability of the North Atlantic Oscillation. *Journal of the Atmospheric Sciences*, *81*(1), 177–208. https://doi.org/10.1175/JAS-D-23-0100.1

Yang, Y., McWilliams, J. C., Liang, X. S., Zhang, H., Weisberg, R. H., Liu, Y. G., & Menemenlis, D. (2021). Spatial and temporal characteristics of the submesoscale energetics in the Gulf of Mexico. *Journal of Physical Oceanography*, *51*(2), 475–489. https://doi.org/10.1175/JPO-D-20-0247.1

Yasuda, I., Yoon, J. H., & Suginohara, N. (1985). Dynamics of the Kuroshio large meander. *Journal of the Oceanographical Society of Japan*, *41*(4), 259–273. https://doi.org/10.1007/BF02109275

Zhang, X., Zhang, Z., McWilliams, J. C., Sun, Z., Zhao, W., & Tian, J. (2022). Submesoscale coherent vortices observed in the northeastern South China Sea. *Journal of Geophysical Research: Oceans*, *127*(2), e2021JC018117. https://doi.org/10.1029/2021JC018117

Zhang, Z. (2024). Submesoscale dynamic processes in the South China Sea. *Ocean-Land-Atmosphere Research*, *3*, 0045. https://doi.org/10.34133/olar.0045

Zhang, Z., & Qiu, B. (2018). Evolution of submesoscale ageostrophic motions through the life cycle of oceanic mesoscale eddies. *Geophysical Research Letters*, *45*(21), 11847–11855. https://doi.org/10.1029/2018GL080399

Zhang, Z., Qiu, B., Klein, P., & Travis, S. (2019). The influence of geostrophic strain on oceanic ageostrophic motion and surface chlorophyll. *Nature Communications*, *10*(1), 2838. https://doi.org/10.1038/s41467-019-10883-w

Zhang, Z., Zhang, Y., Qiu, B., Sasaki, H., Sun, Z., Zhang, X., et al. (2020). Spatiotemporal characteristics and generation mechanisms of submesoscale currents in the northeastern South China Sea revealed by numerical simulations. *Journal of Geophysical Research: Oceans*, *125*(2), e2019JC015404. https://doi.org/10.1029/2019JC015404